Journal of Computational Physics 229 (2010) 4683–4702

Contents lists available at ScienceDirect

Journal of Computational Physics

journal homepage: www.elsevier.com/locate/jcp

Semi-Lagrangian advection–propagation (SLAP) scheme for three-dimensional interface tracking

R.C. Aldredge *

Mechanical and Aeronautical Engineering, University of California, Davis, CA 95616-5294, USA

ARTICLE INFO

Article history:
Received 20 July 2009
Received in revised form 19 February 2010
Accepted 3 March 2010
Available online 15 March 2010

Keywords:
Advection-propagation
Semi-Lagrangian
Surface propagation
Flame
Level-set
Interface tracking

ABSTRACT

A fully three-dimensional semi-Lagrangian scheme is developed for computing the evolution of advected self-propagating surfaces (e.g., premixed flames) governed by a level-set advection–propagation equation. The scheme provides third-order spatial accuracy and shape preservation. Example numerical simulations of three-dimensional front propagation are presented to illustrate the capability of the scheme of capturing cusp formation and associated surface-area annihilation as well as the formation and consumption of detached closed-surface pockets behind fronts propagating in highly vortical flow.

1. Introduction

Markstein and Squire [1] introduced the advection–propagation equation below to describe the propagation of a flame surface through an arbitrary unsteady flow field. This equation governs the evolution of a scalar field $G(\mathbf{x},t)$, describing the motion of any one of its isoscalar surfaces which propagates normal to itself locally while being advected by the flow field $\mathbf{U}(\mathbf{x},t)$

$$\frac{\partial G}{\partial t}+(\mathbf{U}-S_N\mathbf{n})\cdot\nabla G=0. \tag{1}$$

The propagation velocity is $-S_N\mathbf{n}$, where $\mathbf{n}(\mathbf{x},t)\equiv\nabla G/|\nabla G|$ is the local surface normal vector. Thus, the isoscalar surface propagates intrinsically at the speed S_N down the gradient of the scalar field. This is in analogy with the transport of heat by molecular diffusion, which occurs down the gradient of the temperature field. The works of Markstein and Squire [1], Markstein [2] and Williams [3] employed the advection–propagation equation in analytical studies of flame-front stability. Kerstein et al. [4] subsequently used the formulation to investigate attributes of arbitrary-interface propagation in Navier–Stokes turbulence. Osher and Sethian [5] developed the first stable numerical methods for the solution of Eq. (1), also known as the level-set equation, for front propagation in quiescent flow.

In the present work, both S_N and the flow-field velocity $\mathbf{U}$ are measured in units of the known constant planar-surface speed S_L (*e.g.*, the laminar-flame speed); G and the spatial variables ($\mathbf{x}$) are measured in units of a constant length scale l characterizing order-unity variations of the advection field, and time is measured in units of l/S_L. In general, S_N depends locally on properties of the flow field (e.g., the rate of flow-field strain normal to the isoscalar surface) and isoscalar surface geometry

* Tel.: +1 530 752 5016; fax: +1 530 231 2806.
E-mail address: aldredge@ucdavis.edu

0021-9991/$ - see front matter © 2010 Elsevier Inc. All rights reserved.
doi:10.1016/j.jcp.2010.03.006

(*e.g.*, the surface curvature) [1–3,5–7]. However, in the present work the case $S_N = 1$ is considered for simplicity, without a loss of generality of the proposed numerical scheme.

Numerical schemes developed for the accurate solution of Eq. (1) should be shape preserving in the sense that no new local maxima or minima of the scalar field should be created. In other words, although the volume of space between two given isoscalar surfaces will in general vary in time, the range of G over this volume should remain constant. This shape-preservation property is a consequence of the simple fact that the value of G must by definition remain constant along the path of motion of its level set, as determined by its local velocity $\mathbf{v} \equiv \mathbf{U} - S_N\mathbf{n}$ according to Eq. (1). Since $\mathbf{v}$ is not generally solenoidal even when the advection flow-field $\mathbf{U}$ is incompressible (due to the presence of the surface-propagation term), except possibly for the simplest case of planar-surface propagation, G is not generally conserved. A conserved scalar ϕ_{CS}, the integral of which (over the volume of space between two given isoscalar surfaces) remains constant, is governed by the following conservation law

$$\frac{\partial \phi_{CS}}{\partial t} + \nabla \cdot (\phi_{CS}\mathbf{v}) = 0. \tag{2}$$

It can be shown by use of the Reynolds-transport and divergence theorems that any non-propagating scalar field exclusively advected by a solenoidal velocity field is conserved. If the advection flow is compressible, on the other hand, it can be shown in a similar manner that the product of any non-propagating scalar field ψ with the density of the flow ρ is conserved (again assuming no diffusion, production or consumption of the scalar field). In this case, one has $\phi_{CS} = \rho\psi$ and

$$\frac{\partial(\rho\psi)}{\partial t} + \nabla \cdot (\rho\psi\mathbf{U}) = 0, \quad \frac{\partial \psi}{\partial t} + \mathbf{U} \cdot \nabla\psi = 0; \tag{3}$$

the second, advection form of the two relations resulting from mass continuity. An accurate numerical scheme designed to predict the evolution of ψ should be therefore both conservative with regard to $\rho\psi$ and shape-preserving with regard to ψ. Note that the continuity equation, obtained from the first relation in Eq. (3) by setting $\psi = 1$, is not in general shape preserving (except for the trivial case of incompressible flow) because the source term $-\rho\nabla \cdot U$ can cause new maxima or minima in ρ to develop in the flow [8]. Schemes based on Eulerian, control-volume analyses are inherently conservative and have traditionally been popular for solving conservation laws such as Eq. (2) and the first relation of Eq. (3) [8–15]. Semi-Lagrangian schemes which are not inherently conservative but may offer greater computational efficiency over traditional Eulerian methods through the use of larger time steps [16,17] have been attractive for solving advection laws such as the second relation of Eq. (3). Recently, multidimensional schemes which are both conservative and shape-preserving and allow unrestricted time steps have been developed using both Eulerian [13,18,19] and semi-Lagrangian [20,21] formulations. Strain [22] provides an excellent introduction of semi-Lagrangian methods for moving interfaces using time steps unconstrained by numerical-stability issues, including many two-dimensional examples. Ultimately, however, the time step may be limited in many practical simulations by the effect of existing temporal gradients of S_N and $\mathbf{U}$ on the accuracy of isoscalar-surface-element trajectory approximations.

In the present work, we employ a nonconservative shape-preserving semi-Lagrangian scheme for the solution of Eq. (1), consistent with the nonconservative nature of the advection–propagation equation. The scheme is based on a multidimensional formulation which allows for CFL numbers as large as 1. In the following section the formulation of the numerical scheme is presented, followed by examples, discussion and a conclusion in subsequent sections.

2. Formulation

The semi-Lagrangian formulation employed herein for solution of Eq. (1) is derived using upwind transient interpolation modeling (TIM), as described by Leonard et al. [10,14]. Accordingly, the scalar field G at each grid point $\mathbf{x}_{ijk} \equiv (x_i, y_j, z_k)$ is updated at each new time step using the following Lagrangian transport law

$$\left.\begin{aligned} &G(\mathbf{x}_{ijk}, t_n + \Delta t) = G\left(\mathbf{x}^L_{ijk}(t_n), t_n\right), \\ &\mathbf{x}^L_{ijk}(t_n) \equiv \mathbf{x}_{ijk} - \mathbf{v}_{ave}\Delta t, \\ &\mathbf{v}_{ave} = \tfrac{1}{\Delta t}\int_{t_n}^{t_n+\Delta t} \mathbf{v}\left(\mathbf{x}^L_{ijk}(t), t\right) dt. \end{aligned}\right\} \tag{4}$$

Here $\mathbf{x}^L_{ijk}(t)$ is the location at time t of an element of the isoscalar surface on its path from its original location $\mathbf{x}^L_{ijk}(t_n)$ at t_n to its final location $\mathbf{x}_{ijk}$ at $t_n + \Delta t$. In this sense the path defined by $\mathbf{x}^L_{ijk}(t)$ for $t_n \leqslant t \leqslant t_n + \Delta t$ is peculiar to $\mathbf{x}_{ijk}$, being associated with a different surface element at each time step. Since the set of surface elements tracked are not fixed but are redefined at each time step, the transport scheme is characterized as semi-Lagrangian. The value of $\mathbf{x}^L_{ijk}(t_n)$ is specified implicitly by the last two relations of Eq. (4) and is obtained most accurately by iteration if large time steps associated with motion of surface elements over multiple grid cells are to be considered. In the present formulation, we will derive an explicit relation for $\mathbf{x}^L_{ijk}(t_n)$ but prevent surface elements from completely traversing more than one grid cell during a given time step to preserve accuracy. Consequently, the local CFL number based on the magnitude of the surface-element velocity $\mathbf{v} \equiv \mathbf{U} - S_N\mathbf{n}$ and the grid spacing Δx will be limited to a value of no greater than 1.

Expanding $\mathbf{v}$ about t_n in the last relation of Eq. (4) results in the following second-order approximation for the local average surface-element velocity $\mathbf{v}_{ave}$.

$$\mathbf{v}_{ave} = \mathbf{v}\left(\mathbf{x}^L_{ijk}(t_n), t_n\right) + \frac{1}{2}\Delta t\left[\frac{\partial \mathbf{v}}{\partial t} + (\mathbf{v}\cdot\nabla)\mathbf{v}\right]\left(\mathbf{x}^L_{ijk}(t_n), t_n\right) + O((\Delta t)^2). \tag{5}$$

Then, expanding the surface-element velocity and its derivatives at the upstream point of departure $\mathbf{x}^L_{ijk}(t_n)$ about their respective values at $\mathbf{x}_{ijk}$ using the second relation of Eq. (4) gives the following explicit second-order relation for $\mathbf{v}_{ave}$

$$\mathbf{v}_{ave} = \mathbf{v}(\mathbf{x}_{ijk}, t_n) + \frac{1}{2}\Delta t\left[\frac{\partial \mathbf{v}}{\partial t} - (\mathbf{v}\cdot\nabla)\mathbf{v}\right](\mathbf{x}_{ijk}, t_n) + O((\Delta t)^2). \tag{6}$$

However, approximation of the spatial gradients in this expression will introduce additional errors of order $\Delta t(\Delta x)^m$, where m is the order of the spatial-difference errors. We will use a first-order backward difference for the time derivative and a fourth-order difference for the spatial gradients, as given for G in the first relation of Eq. (8) below, making the relation for $\mathbf{v}_{ave}$ ultimately of $O(\Delta t(\Delta x)^4, (\Delta t)^2)$.

To obtain the equation for updating G at each new time step, we need only now to expand the right-hand side of the first relation of Eq. (4) about $\mathbf{x}_{ijk}$. This is accomplished using the following polynomial interpolation of G at points x in a continuous cubic space of volume $(\Delta x)^3$ centered at $\mathbf{x}_{ijk}$

$$G(\mathbf{x}, t_n) = G(\mathbf{x}_{ijk}, t_n) + \xi_p \frac{\partial G}{\partial \xi_p}(\mathbf{x}_{ijk}, t_n) + \frac{1}{2}\xi_p\xi_q \frac{\partial^2 G}{\partial \xi_p \xi_q}(\mathbf{x}_{ijk}, t_n) + \frac{1}{6}\xi_p\xi_q\xi_r \frac{\partial^3 G}{\partial \xi_p \xi_q \xi_r}(\mathbf{x}_{ijk}, t_n) + O\left((\xi_p\xi_p)^2\right). \tag{7}$$

In this relation ξ_p is any one of the three components of the distance vector $\mathbf{x} - \mathbf{x}_{ijk}$, and summation is implied by repeated indices in accordance with common tensor notation. The interpolation, valid for $-\Delta x/2 \leqslant \xi_p \leqslant \Delta x/2$, is collocated on an upwind-biased three-dimensional stencil of grid points following Leonard *et al.* [14], resulting in the following expansions of the spatial gradients

$$\left.\begin{aligned}
&\tfrac{\partial G}{\partial \xi_p}(\mathbf{x}_{ijk}, t_n) = \tfrac{1}{\Delta x} sign(c_p)\left(\delta_p - \tfrac{1}{6}\delta_p^{(u)} D_p\right)G + O((\Delta x)^4),\\
&\tfrac{\partial^2 G}{\partial \xi_p \partial \xi_q}(\mathbf{x}_{ijk}, t_n) = \tfrac{1}{2(\Delta x)^2} sign(c_p) sign(c_q)\left(\delta_q^{(u)}\delta_p^{(d)} + \delta_p^{(u)}\delta_q^{(d)}\right)G + O((\Delta x)^2),\\
&\tfrac{\partial^3 G}{\partial \xi_p^2 \partial \xi_q}(\mathbf{x}_{ijk}, t_n) = \tfrac{1}{(\Delta x)^3} sign(c_q)\delta_q^{(u)} D_p G + O(\Delta x),\\
&\tfrac{\partial^3 G}{\partial \xi_p \partial \xi_q \partial \xi_r}(\mathbf{x}_{ijk}, t_n) = \tfrac{1}{(\Delta x)^3} sign(c_p) sign(c_q) sign(c_r)\delta_p^{(u)}\delta_q^{(u)}\delta_r^{(u)} G + O(\Delta x),\\
&\qquad (p, q, r \ \textit{all distinct}).
\end{aligned}\right\} \tag{8}$$

In these relations $\delta_p^{(u)}$ ($\delta_p^{(d)}$) is a first-order upwind (downwind) difference operator, and δ_p and D_p are first- and second-order central-difference operators, respectively, acting on G along the p^{th} coordinate of $\mathbf{x}$. For example, for $p = 1$, one has

$$\left.\begin{aligned}
&\delta_x^{(u)} G = G_{ijk} - G_{iu,j,k}, \quad \delta_x^{(d)} G = G_{id,j,k} - G_{ijk},\\
&\delta_x G = \tfrac{1}{2}\left(\delta_x^{(u)} + \delta_x^{(d)}\right)G = \tfrac{1}{2}(G_{id,j,k} - G_{iu,j,k}),\\
&D_x G = \delta_x^{(u)}\delta_x^{(d)} = G_{iu,j,k} - 2G_{ijk} + G_{id,j,k},
\end{aligned}\right\} \tag{9}$$

where $iu = i - sign(c_x)$ and $id = i + sign(c_x)$ are the grid points immediately upstream and downstream of $\mathbf{x}_{ijk}$, respectively, along the x axis. Components of the normalized average surface-element velocity $\mathbf{v}_{ave}\Delta t/\Delta x$ are represented by c_p (either c_x, c_y or c_z), with the sign of c_p approximated as $sign(c_p(\mathbf{x}_{ijk}, t_n))$. The second and third relations of Eq. (8) are valid for both $p = q$ and $p \neq q$, while the last is valid only when no two of the three indices are equal.

Specifying $\mathbf{x} = \mathbf{x}^L_{ijk}(t_n)$ in Eq. (7), so that ξ_p becomes a component of $-\mathbf{v}_{ave}\Delta t$, gives the following

$$G\left(\mathbf{x}^L_{ijk}(t_n), t_n\right) = \left(G - c_p(\Delta x)\frac{\partial G}{\partial \xi_p} + \frac{1}{2}c_p c_q(\Delta x)^2 \frac{\partial^2 G}{\partial \xi_p \xi_q} - \frac{1}{6}c_p c_q c_r(\Delta x)^3 \frac{\partial^3 G}{\partial \xi_p \xi_q \xi_r}\right)\Bigg|_{(\mathbf{x}_{ijk}, t_n)} + O((\Delta x)^4). \tag{10}$$

Introducing the upwind-biased spatial derivatives of G specified in Eq. (8) then gives

$$\begin{aligned}
G\left(\mathbf{x}^L_{ijk}(t_n), t_n\right) = G(\mathbf{x}_{ijk}, t_n) &- \frac{1}{2}|c_p|\left[|c_p c_q|\delta_q^{(u)} - \frac{1}{3}\left(1 + 2c_p^2\right)\delta_p^{(u)}\right]D_p G\\
&- \left[|c_p|\delta_p - \frac{1}{4}|c_p c_q|\left(\delta_q^{(u)}\delta_p^{(d)} + \delta_p^{(u)}\delta_q^{(d)}\right) + \frac{1}{6}|\varepsilon_{pqr} c_p c_q c_r|\delta_p^{(u)}\delta_q^{(u)}\delta_r^{(u)}\right]G + O((\Delta x)^4),
\end{aligned} \tag{11}$$

where ε_{pqr} is the Levi–Civita tensor, the absolute value of which equals 1 when p, q and r are all distinct and 0 otherwise. Expansion of Eq. (11), and consideration of the first relation of Eq. (4), results in the following

$$
\begin{aligned}
G(\mathbf{x}_{ijk}, t_n + \Delta t) = G(\mathbf{x}_{ijk}, t_n) &- \Big[(|c_x|\delta_x + |c_y|\delta_y + |c_z|\delta_z) + |c_x c_y c_z|\delta_x^{(u)}\delta_y^{(u)}\delta_z^{(u)}\Big]G \\
&+ \frac{1}{2}\Big[|c_x c_y|\Big(\delta_x^{(u)}\delta_y^{(d)} + \delta_y^{(u)}\delta_x^{(d)}\Big) + |c_x c_z|\Big(\delta_x^{(u)}\delta_z^{(d)} + \delta_z^{(u)}\delta_x^{(d)}\Big) + |c_y c_z|(\delta_y^{(u)}\delta_z^{(d)} + \delta_z^{(u)}\delta_y^{(d)})\Big]G \\
&+ \frac{1}{2}|c_x|\Big[|c_x|\Big(1 - |c_y|\delta_y^{(u)} - |c_z|\delta_z^{(u)}\Big) + \frac{1}{3}\left(1 - c_x^2\right)\delta_x^{(u)}\Big]D_x G \\
&+ \frac{1}{2}|c_y|\Big[|c_y|\Big(1 - |c_x|\delta_x^{(u)} - |c_z|\delta_z^{(u)}\Big) + \frac{1}{3}\left(1 - c_y^2\right)\delta_y^{(u)}\Big]D_y G \\
&+ \frac{1}{2}|c_z|\Big[|c_z|\Big(1 - |c_x|\delta_x^{(u)} - |c_y|\delta_y^{(u)}\Big) + \frac{1}{3}\left(1 - c_z^2\right)\delta_z^{(u)}\Big]D_z G + O((\Delta x)^4)
\end{aligned}
\tag{12}
$$

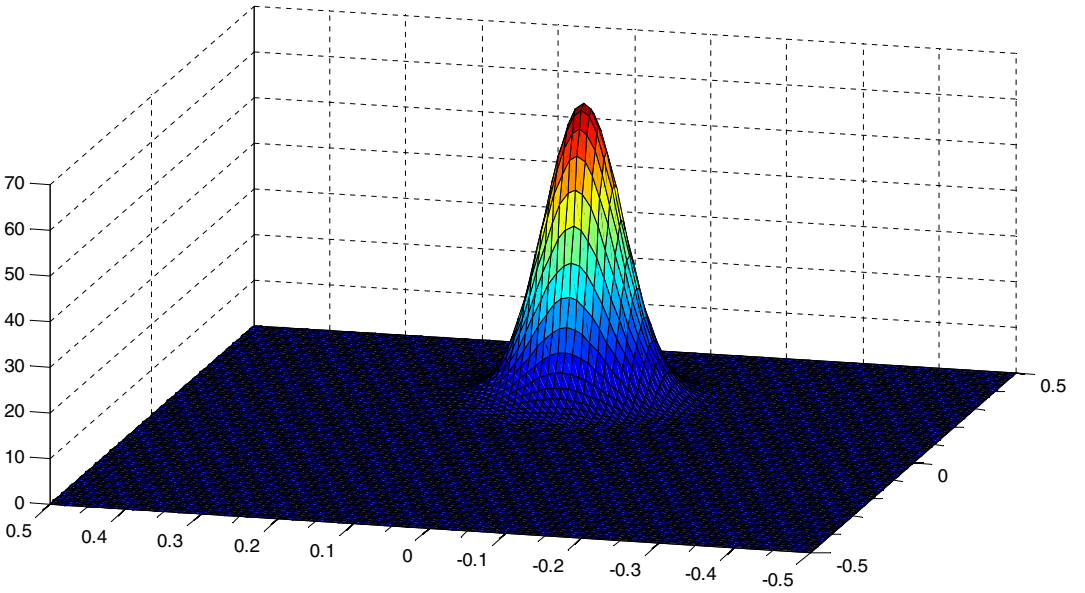

Fig. 1(a). The initial Gaussian distribution, with 5% standard deviation, centered at (0,0.25) on a grid with 100×100 computational nodes.

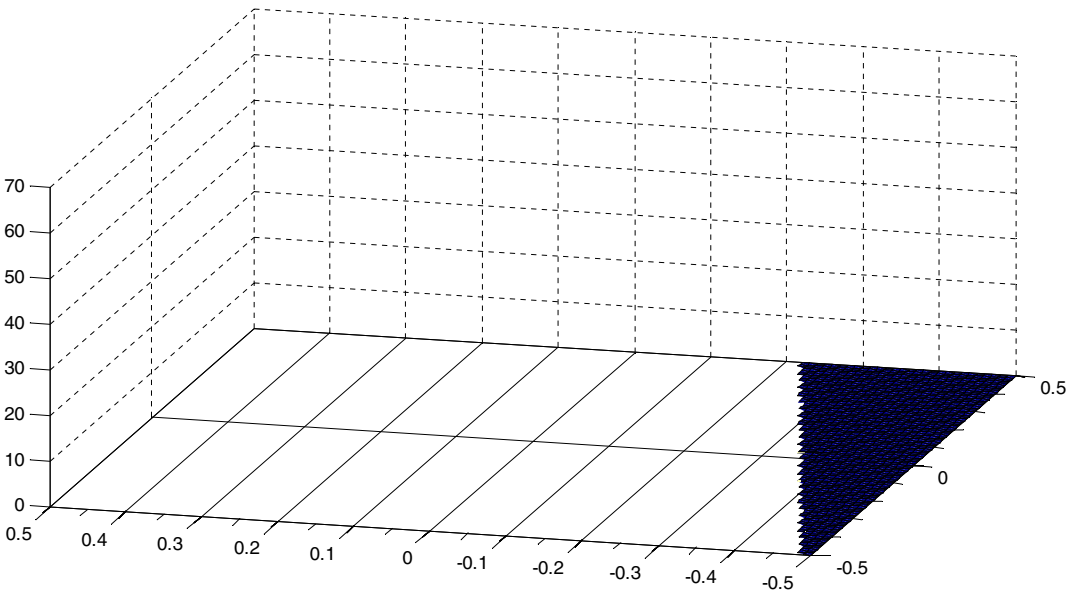

This result agrees identically with that represented in Eqs. (A.1.1)–(A.1.22) of Leonard et al. [14], with the errors in Eqs. (A.1.15) and (A.1.18) corrected, as must be the case since the twenty-node upstream-biased stencil proposed in Fig. A.1.1 therein was chosen for collocation of our interpolation of G. It should be noted, however, that the direct application of Eq. (12) in the SLAP algorithm presented herein for the solution of the non-conservative advection–propagation equation, Eq.

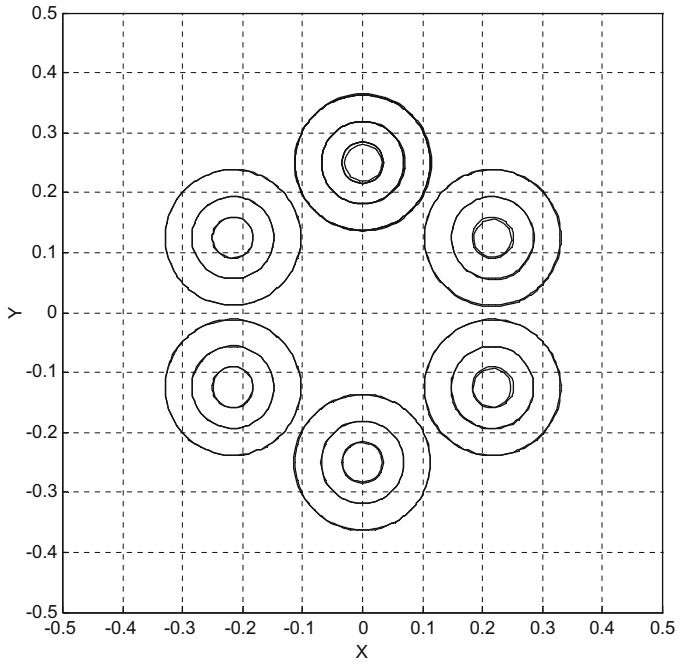

Fig. 2. Contours of the calculated Gaussian distribution (dotted lines) at six equal intervals of the revolution of rotation, compared with the exact evolution of the initial distribution (solid lines). Isolevel distribution heights of 5, 25 and 50 are shown.

Table 1
Errors obtained for the simulations of the Gaussian distribution subjected to rigid-body rotation.

# Nodes	Δx	Δt	CFL	Max error	Ave error	Error ratio
50×50	2.00E−02	2.25E−03	5.00E−01	2.05E+01	1.97E−01	
100×100	1.00E−02	2.25E−03	1.00E+00	6.33E+00	2.58E−02	7.64E+00
50×50	2.00E−02	1.13E−03	2.50E−01	2.12E+01	2.04E−01	
100×100	1.00E−02	1.13E−03	5.00E−01	7.35E+00	3.00E−02	6.80E+00
200×200	5.00E−03	1.13E−03	1.00E+00	1.69E+00	3.39E−03	8.83E+00

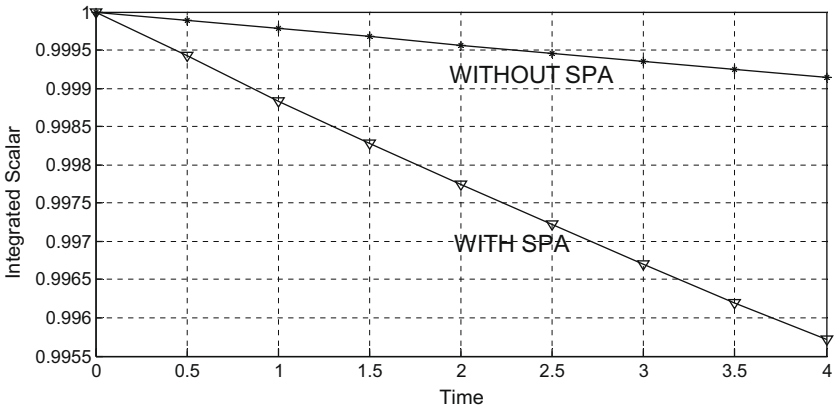

Fig. 3. The calculated integration of the Gaussian distribution plotted over four periods of counterclockwise rigid-body rotation, with and without implementation of the shape-preserving algorithm (SPA).

(1), differs from the application of Eq. (12) by Leonard et al. [14] in their Eulerian algorithm for the solution of conservation laws of the form of Eq. (2). The formulation of Leonard et al. [14] involves splitting the differences on the right-hand side of Eq. (12) into six groups of symmetrical cell-interface fluxes and employing first-order spatial approximations for the normalized average surface-element velocities c_p (ascribed to the disparate cell interfaces). Their formulation is consequently formally valid only for applications involving spatially uniform c_p unlike the formulation presented herein, which employs the more general form of the TIM updating algorithm expressed in Eq. (12) and is valid for propagating interfaces (typically having highly non-uniform surface-element velocities).

The errors of the approximation of $G(\mathbf{x}_{ijk}, t_n + \Delta t)$ given in Eq. (12) become ultimately third order in space, when the approximations for c_x, c_y and c_z obtained from Eq. (6) by multiplication with $(\Delta t)/(\Delta x)$ are introduced. The approximation may be limited to ensure shape preservation (monotonicity). To this end, we examine the influence of a shape-preservation algorithm (SPA) requiring that the scalar update $G(\mathbf{x}_{ijk}, t_n + \Delta t)$ be no greater (less) than the largest (smallest) of the scalar values at t_n at the eight corners of the cubic octant immediately upstream of $\mathbf{x}_{ijk}$. For example, if all components of $\mathbf{v}_{ave}$ are positive then these corners are at $\mathbf{x}_{ijk}$, $\mathbf{x}_{i-1,j,k}$, $\mathbf{x}_{i,j-1,k}$, $\mathbf{x}_{i-1,j-1,k}$, $\mathbf{x}_{ijk-1}$, $\mathbf{x}_{i-1,j,k-1}$, $\mathbf{x}_{i,j-1,k-1}$, and $\mathbf{x}_{i-1,j-1,k-1}$. The results of our simulations show, however, that both shape preservation and scalar-field conservation are essentially obtained without the

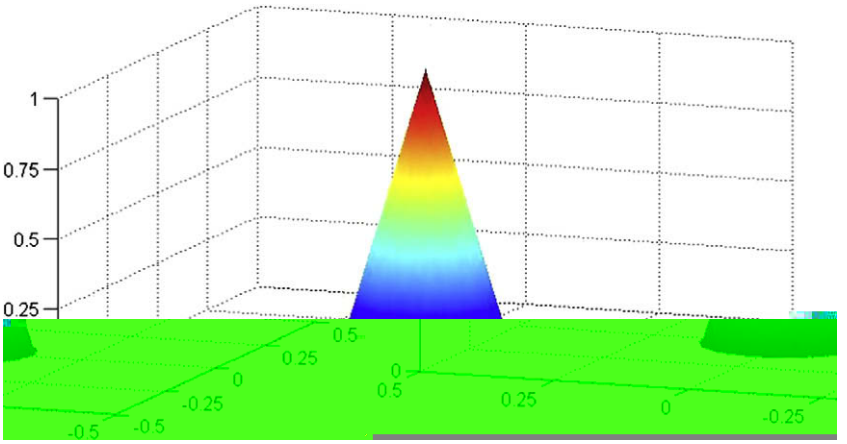

Fig. 4(a). The initial conical distribution, centered at the origin (0,0).

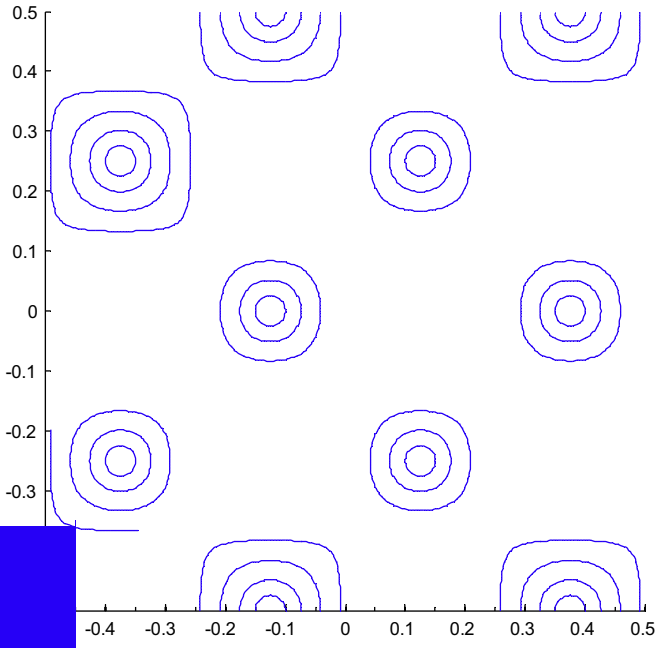

implementation of the SPA for the cases of pure solenoidal-velocity advection considered (with the necessity in some cases of a slightly reduced CFL number) – as discussed below.

3. Examples

As a first example, we consider two-dimensional advection of a Gaussian distribution in the plane (x,y) of its base. The distribution, having a standard deviation of 5%, is initially centered on the y axis at $(0,0.25)$ in a computational domain of unit square area defined by $(-0.5 \leqslant x \leqslant 0.5)$ and $(-0.5 \leqslant y \leqslant 0.5)$ and subjected to counterclockwise rigid-body rotation with a time period of unity. The CFL number $umax \times \Delta t/\Delta x$ is set to 1, so that $\Delta t = \Delta x/\sqrt{2}\pi$ since $umax = 2\pi \cdot r_{max}$ (where $r = sqrt(x^2 + y^2)$). Figs. 1(a) and 1(b) show the initial distribution and the distribution after one complete revolution of rotation, on a grid with 100×100 computational nodes. Although there is slight attenuation of the peak of the distribution after one revolution, the advection routine is clearly stable, without the formation of local minima or maxima. Fig. 2 shows the contours of the numerically calculated distribution in the (x,y) plane at six equal intervals of the revolution, compared with the exact evolution (represented by the solid lines). It is clear that the symmetry of the calculated distribution is maintained by our multidimensional scheme, in contrast with the performance of traditional time-splitting algorithms. The average error between the calculated and exact distributions over the revolution period is presented in Table 1. The last column of the table represents the inverse of the ratio of the average error obtained for the parameters specified in a given row to that obtained for the parameters in the previous row. For example, the average error obtained when 50×50 computational nodes are used with a CFL number of 0.5 is 7.64 times that obtained when 100×100 nodes are used with a CFL number of 1 (and the same time step), representing essentially third-order spatial accuracy. Similarly, the average error obtained when 100×100 computational nodes are used is 8.83 times that obtained when 200×200 nodes are used with the same time step, again representing third-order spatial accuracy. Finally, the influence of the SPA on mass conservation is shown in Fig. 3, where the integration of the scalar G over the computational domain is plotted versus time over four periods of rigid-body rotation. Since the flow field is solenoidal the integrated scalar should remain equal to its initial value of 1. Although this is not the case in the strictest sense, only very minor attenuation occurs with increasing time – with a loss of less than 0.5% (0.1%) when the SPA is turned on (off). For these simulations, the CFL number was reduced to 0.75 for both cases (so as to ensure stability without the SPA). A computational grid with 200×200 nodes was used, giving average errors over the long-time simulations of 0.016 and 0.014 for the cases with and without the SPA, respectively. Hence, conservation of the total scalar mass is essentially achieved without the SPA, with no loss of computational accuracy.

In the next example, we compute the evolution of a conical distribution distorted by a field of counter-rotating vortices in the plane of its base, as described by Smolarkiewicz [23]. As shown in Fig. 4(a), the cone of unit height is initially centered on a computational domain identical to that of the previous example. Its contours are shown in Fig. 4(b), along with the streamlines of the steady vortical flow field (u, v) given by

$$\left.\begin{aligned} \psi &= A\sin(kx)\cos(ky),\\ u &= -\partial\psi/\partial y = kA\sin(kx)\sin(ky),\\ v &= \partial\psi/\partial x = kA\cos(kx)\cos(ky), \end{aligned}\right\} \tag{13}$$

with $A = 8$ and $k = 4\pi$. The cone is positioned such that a vortex rotating clockwise (counterclockwise) is centered 0.125 units to the right (left) of the center of the cone. Each of the vortices is confined to a square cell of 0.25 units in width, with

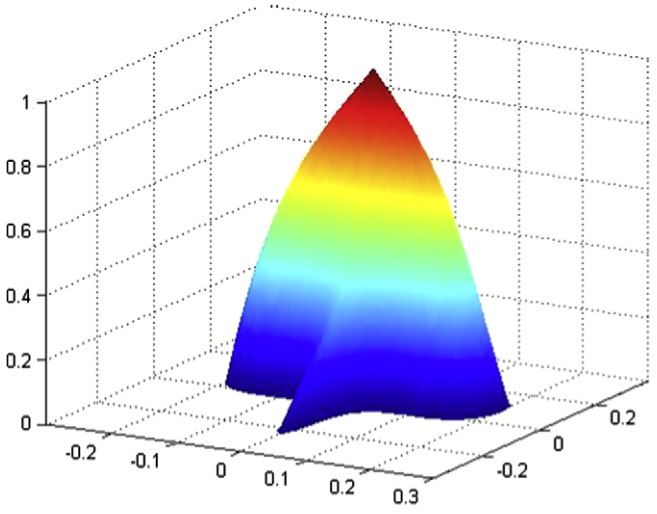

Fig. 5(a). The exact evolution of the initially conical distribution after $0.25P_c$ time units.

no flow across the cell walls. Since the diameter of the cone base (0.3 units) is slightly greater than the vortex cell width it is expected that the initial conical distribution will be partially advected into the cells immediately above and below. However, the distribution will remain symmetrical about the vertical axis passing through the origin and confined to the six central cells (closest to the origin).

First, an analytical solution of the distribution evolution is obtained using the method presented by Staniforth et al. [24]. Specifically, a linear translation of the original (x,y) coordinate system to one (θ,λ) having its origin at the lower left corner of each vortex cell is made. Then, Lagrangian equations of motion for the coordinates $[\theta(t),\lambda(t)]$ of a given fluid element after advection from their initial values at $t = 0$ are derived and solved analytically. In summary, one has

$$\left.\begin{aligned} &\theta \equiv kx - n\pi, \\ &\lambda \equiv ky - \left(l - \tfrac{1}{2}\right)\pi, \\ &d^2\theta/dt^2 = (k^2A)^2 \sin\theta\cos\theta, \\ &d^2\lambda/dt^2 = (k^2A)^2 \sin\lambda\cos\lambda, \end{aligned}\right\} \tag{14}$$

where the values of the integral parameters n and l, ranging from -2 to 2 in this case, are defined for each vortical cell so as to keep both θ and λ in the range between 0 and π over the entire computational domain. Solutions to the evolution equations in Eq. (14) are given by

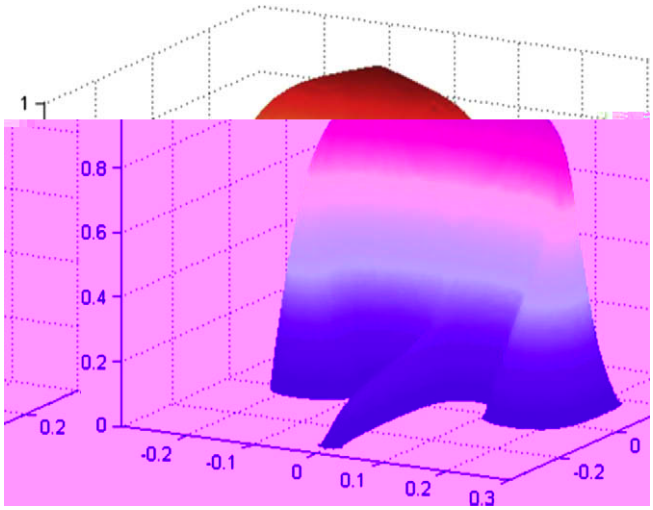

Fig. 5(b). The exact evolution of the initially conical distribution after $0.5P_c$ time units.

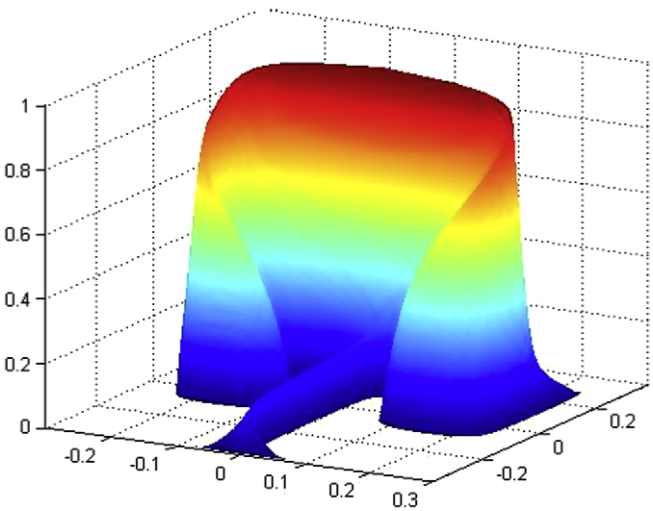

Fig. 5(c). The exact evolution of the initially conical distribution after $0.75P_c$ time units.

$$\left.\begin{aligned}
&\theta = \cos^{-1}\left(m^{1/2} sn\left[-\sigma_u A k^2 (t - t_0) + C_u, m\right]\right), \\
&\lambda = \cos^{-1}\left(m^{1/2} sn\left[-\sigma_v A k^2 (t - t_0) + C_v, m\right]\right), \\
&\sigma_u \equiv sign(u(x_0, y_0), \sigma_v \equiv sign(v(x_0, y_0)), \\
&m \equiv 1 - (\psi(x_0, y_0)/A)^2,
\end{aligned}\right\} \tag{15}$$

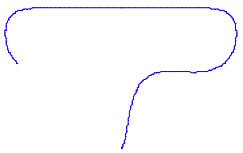

where $sn[z,m]$ is the Jacobian elliptic function and the constants C_u and C_v are determined from the initial conditions; namely, $sn[C_u,m]=\cos(\theta_0)/m^{1/2}$ and $sn[C_v,m]=\cos(\lambda_0)/m^{1/2}$, respectively (requiring the inverse of sn) [24]. Although Eq. (15) provides exact solutions for the locations of advected fluid elements at arbitrarily large times from known initial conditions, to obtain accurate analytical solutions we have found it necessary to employ multiple small time steps (*e.g.*, 5% of the total time) so as to assure that at each time step σ_u and σ_v are determined at locations sufficiently close to the new advection locations. With the new advection location (x_{new},y_{new}) of each computational node (x_0,y_0) of the original cone base determined from the calculated values of θ and λ, by application once more of the first two relations of Eq. (14), the evolution of the distribution at a given time is then given by $\phi_0(x_{new}(x_0,t),y_{new}(x_0,t))$, where $\phi_0(x,y)\equiv\phi(x,y,t=0)$ is the initial conical

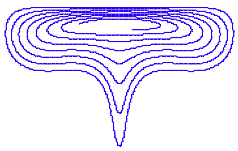

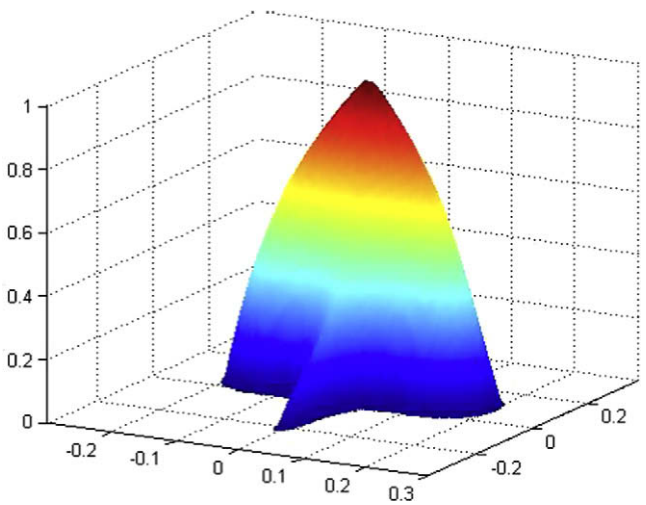

Fig. 8(a). The numerical evolution of the initially conical distribution after $0.25P_c$ time units.

distribution. Figs. 5(a),5(b),5(c),5(d) show snapshots of the exact evolution of the initially conical distribution, obtained as described above, at four times equal to $0.25P_c,\ 0.5P_c,\ 0.75P_c$ and P_c; where $P_c = 2\pi/(k^2A) = (64\pi)^{-1}$ is the period of a fluid element advected around a vortex center obtained in the asymptotic limit in which the initial distance from the vortex center vanishes. The contours of the exact distribution evolution at corresponding times are plotted in Fig. 6.

For the numerical calculation, we used a uniform grid with 400x400 nodes over the entire computational domain and a CFL number of 1, based on the maximum magnitude of the vortical velocity field specified in Eq. (13). Fig. 7 shows the contours of the calculated distribution at the same times as those of the analytically determined distribution evolutions presented in Figs. 5(a),5(b),5(c),5(d), 6. In comparing Figs. 6 and 7, we find that the contours of the numerical solutions are almost identical to those of the exact analytical solutions. Only small differences are notable between the contours of the two solutions at the largest time, P_c, where the upward extension of the horns of the numerical solution (at $x = \pm 0.25,\ y = 0.125$) is not as great. Snapshots of the numerically calculated distribution are presented in Figs. 8(a),8(b),8(c),8(d). Agreement between these and the analytically calculated distributions presented in Figs. 5(a),5(b),5(c),5(d) is generally good except for marked attenuation of the computed profiles near the cone tip (stretched across the computational domain laterally) with increasing time, likely due to the lower resolution of the uniform grid used in the semi-Lagrangian simulation in comparison with that of the highly nonuniform grid that is germane to the true-Lagrangian analytical solution method outlined above. This attenuation is severe after P_c time units, even though the rest of the computed profile away from the tip of the initial conical distribution compares well with that of the analytically determined solution. Fig. 9(a) shows a long-time evolution of the distribution, after $4P_c$ time units; while the contours of the distribution at times of $P_c,\ 2P_c,\ P_c$ and $4P_c$ are shown in Fig. 9(b). It is clear that the calculation is stable and shape preserving

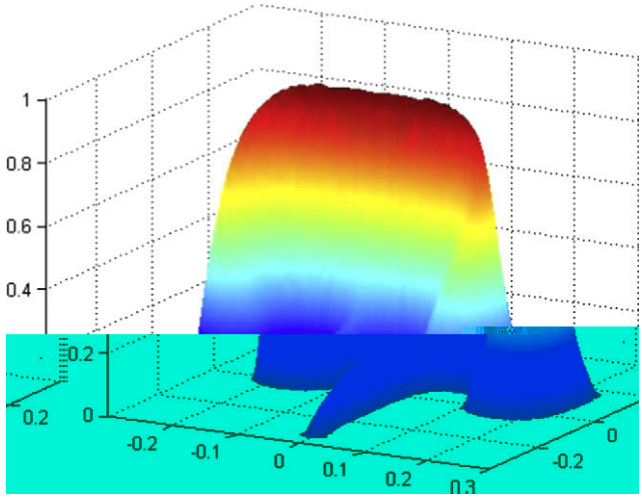

Fig. 8(b). The numerical evolution of the initially conical distribution after $0.5P_c$ time units.

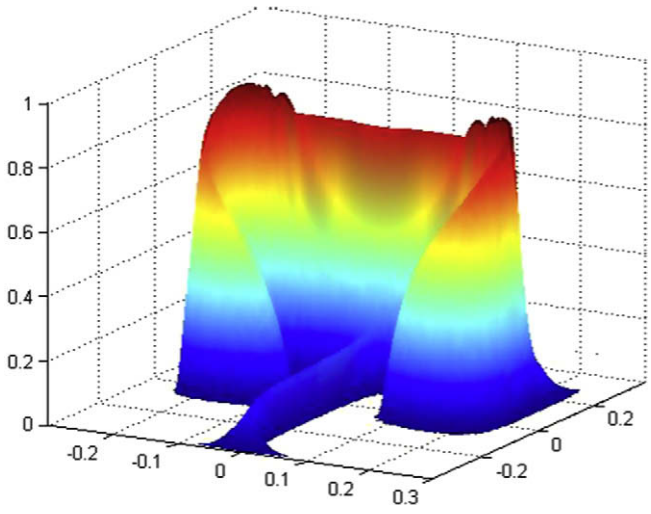

Fig. 8(c). The numerical evolution of the initially conical distribution after $0.75P_c$ time units.

even after $4P_c$ units of time when very strong deformation of the scalar field is evident. The influence of the SPA on mass conservation is shown in Fig. 10, where the integration of the initially conical distribution over the computational domain divided by its initial value is plotted versus time, measured in units of P_c. Since the vortical flow field used in this example, given by Eq. (13), is solenoidal the calculated scalar should be conserved, its integration over the computational domain remaining constant. Although this is not the case, only minor changes in the integrated scalar (less than 1%) are found with implementation of the SPA for times up to P_c. However, the SPA is associated with more significant errors in the integrated scalar for times greater than P_c, although remaining less than 10% for simulation times up to $4P_c$. Without the SPA the advected scalar is essentially conserved over the entire long-time simulation, until $4P_c$ time units, with variations of the integrated scalar from its initial value remaining less than 0.2%. It should be noted that there were no substantial visual differences between the calculated scalar distribution at $4P_c$ time units without implementation of the SPA and the distribution calculated with the SPA (shown in Fig. 9(a)). Hence, conservation of the total scalar mass is essentially achieved without the SPA, with no substantial loss of shape preservation, as was the case with the previous example involving the rotated Gaussian distribution.

The final two examples involve three-dimensional front propagation governed by Eq. (1). In the first example we compute the evolution of an initially wrinkled quasiplanar surface propagating through a quiescent flow ($\mathbf{U} = \mathbf{0}$). The local normal front speed is assumed to be constant, so that $S_N = 1$, and the initial distribution of the scalar field is defined by

$$G(\mathbf{x}, t = 0) = x + 0.1\cos(ky)\sin(kz); \tag{16}$$

where $k = 4\pi$ as in the previous example. Each front is an isoscalar surface defined by a specific constant value of G. For example, $G = 0$ represents a wrinkled quasiplanar front with sinusoidal perturbations about the $y - z$ plane ($x = 0$) at $t = 0$

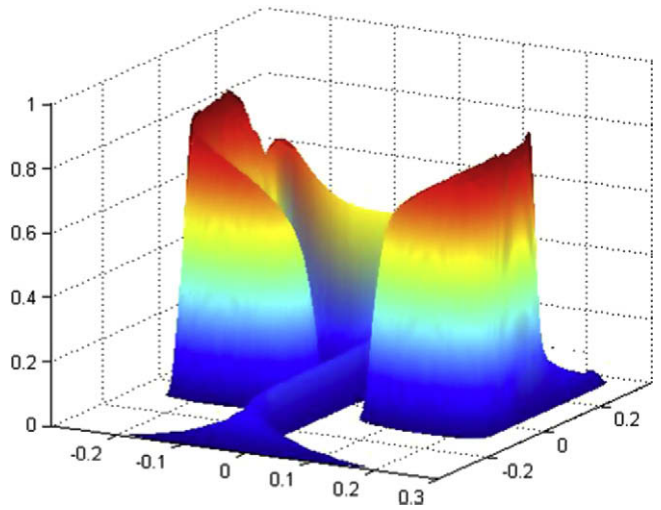

Fig. 8(d). The numerical evolution of the initially conical distribution after P_c time units.

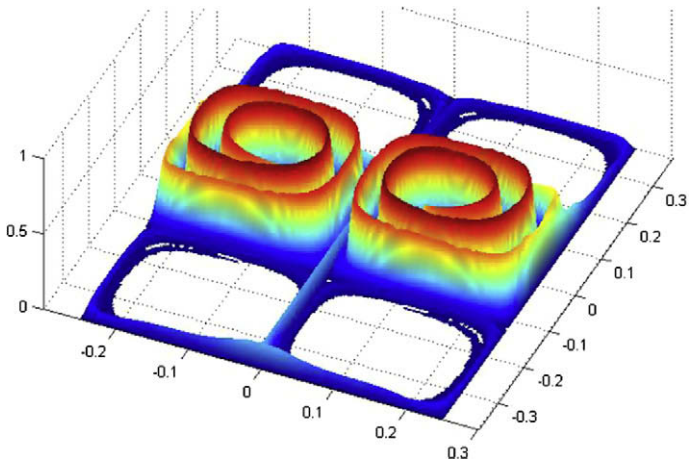

Fig. 9(a). The numerical evolution of the initially conical distribution after $4P_c$ time units.

according to Eq. (16). The average location of this front (initially $x = 0$) will move down the average gradient of the scalar field G. At any given time the average front location is equal to $-\langle G(x = 0)\rangle_{y,z}$, where the brackets denote spatial averaging over the $y - z$ plane. This is true for any quasiplanar front that can be characterized by a scalar field of the form $G = x + f(y, z, t)$,

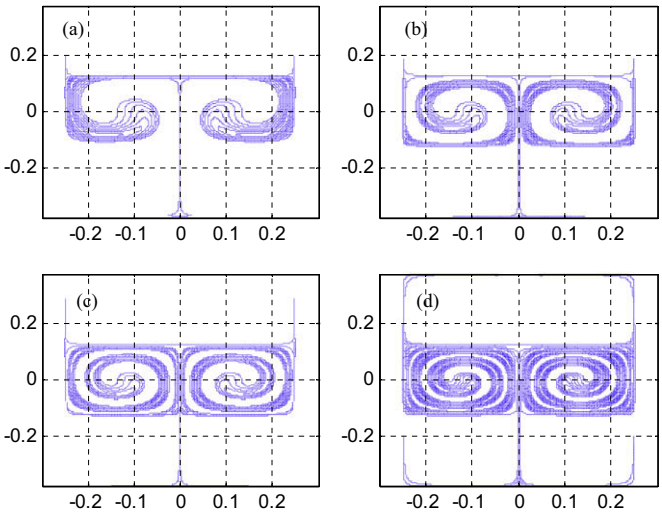

Fig. 9(b). Contours of the calculated long-time evolution of the initially conical distribution at times: (a) P_c, (b) $2P_c$, (c) $3P_c$, (d) $4P_c$.

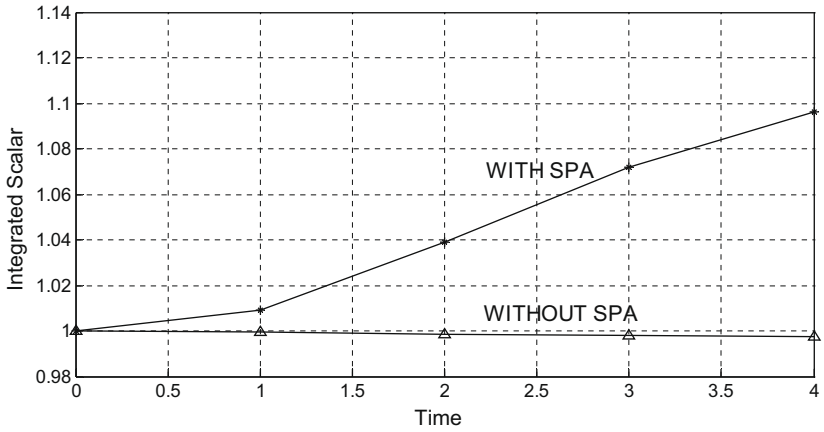

Fig. 10. The calculated long-time integration of the initially conical distribution, normalized with its initial value, plotted versus time with and without implementation of the shape-preserving algorithm (SPA); time is measured in units of P_c.

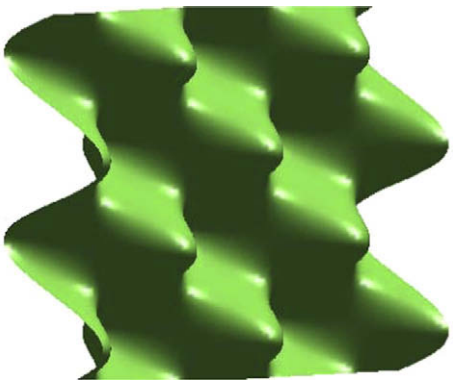

Fig. 11(a). The initially sinusoidal isoscalar front $G = 0$.

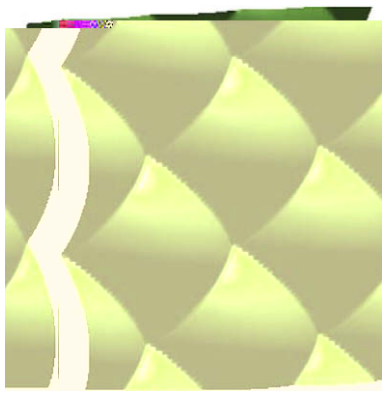

Fig. 11(b). The evolution of the initially sinusoidal isoscalar front $G = 0$ after 0.5 time units.

Fig. 11(c). The evolution of the initially sinusoidal isoscalar front $G = 0$ after 1 time unit.

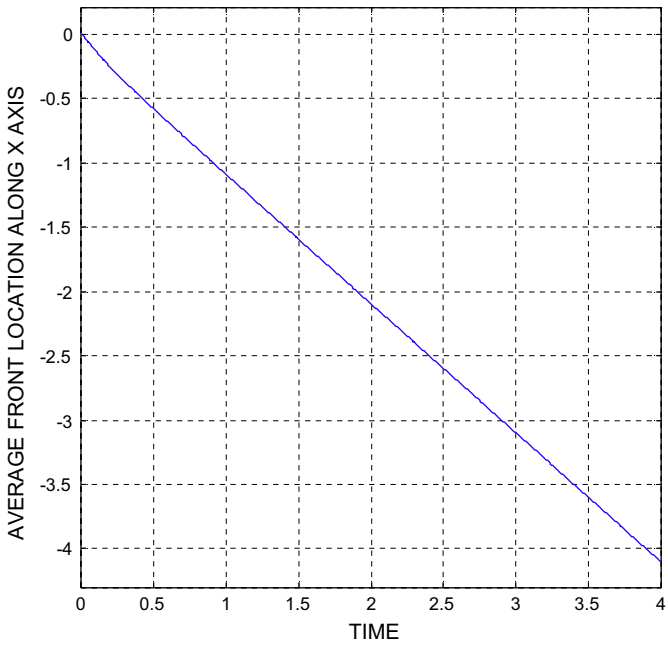

Fig. 12. The average front location along the x axis plotted versus time

since in this case the average location of the isoscalar $G = 0$ along the x axis at any given time is $-\langle f \rangle_{y,z}$ which equals $-\langle G(x = 0) \rangle_{y,z}$. The average global speed of the front, equal to $d\langle G(x = 0) \rangle_{y,z}/dt$ in this case, is in general greater than the local normal front speed ($S_N = 1$) because of the increased surface area

Figs. 11(a),11(b),11(c) show the front at $t = 0$, defined by Eq. (16), and at 0.5 and 1 time units later; computed on a computational grid with $100 \times 100 \times 100$ nodes. The CFL number was set equal to 1 based on S_L, so that $dt = dx = 0.01$ in non-dimensional units. Initially, the surface of the front is smooth everywhere. However, cusps develop on the surface early on (by 0.1 time units), a well known consequence of the Huygens principal of advancing wave fronts [25]. Cusp formation results in surface-area annihilation (associated with the constant local normal front speed in this case). This becomes evident upon comparison of Figs. 11(b) and 11(c), the latter showing significant attenuation of the amplitude of surface wrinkles relative to that at the earlier time. Associated with the decrease in surface area during front propagation after cusp formation is

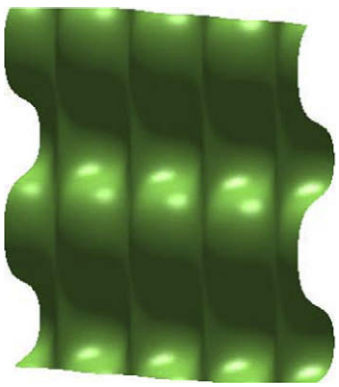

Fig. 13(a). The initially planar front after $0.25P_c$ time units of propagation and advection by the vortical flow field.

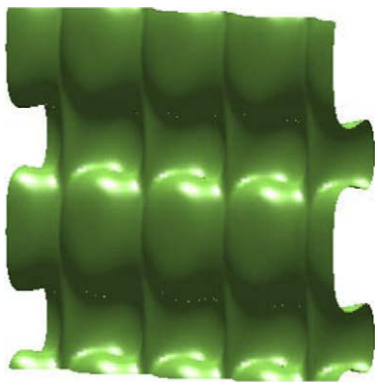

Fig. 13(b). The initially planar front after $0.375P_c$ time units of propagation and advection by the vortical flow field.

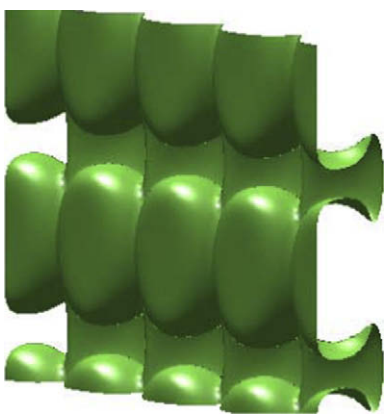

Fig. 13(c). The initially planar front after $0.5P_c$ time units of propagation and advection by the vortical flow field.

a decrease in the average front speed with time. This is evident upon examination of the plot of the average front position along the x axis with time in Fig. 12, the slope of which decreases in magnitude during the early stage of propagation. As the front becomes more and more planar at large times its speed approaches the constant local normal front speed S_L.

In the second example of three-dimensional front propagation, we compute the evolution of an initially planar front propagating locally at S_L through a steady, incompressible vortical flow – according to Eq. (1), with $S_N = S_L = 1$ in this case. Initially, the front lies in the $y - z$ plane at $x = 0.125$, corresponding to the isoscalar $G = 0.125$ of an initial scalar distribution defined by $G(x, t = 0) = x$. The flow field, as defined below, has components in the $x - z$ plane only but varies spatially along all three coordinate directions

$$\left.\begin{aligned} u &= 4\sin(4\pi x)\cos(4\pi y)\sin(4\pi z),\\ v &= 0,\\ w &= 4\cos(4\pi x)\cos(4\pi y)\cos(4\pi z). \end{aligned}\right\} \tag{17}$$

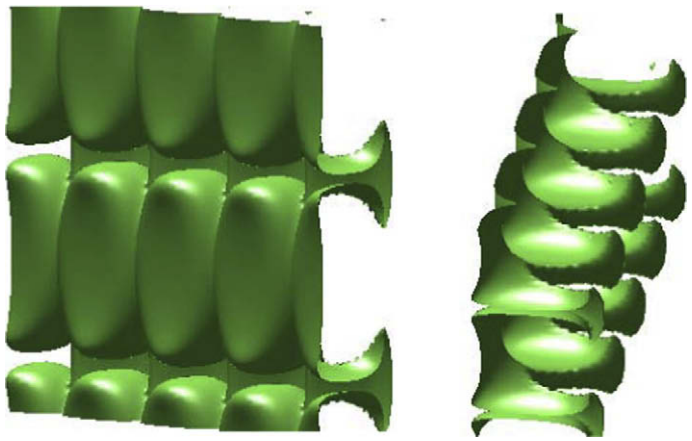

Fig. 13(d). The initially planar front after $0.625P_c$ time units of propagation and advection by the vortical flow field.

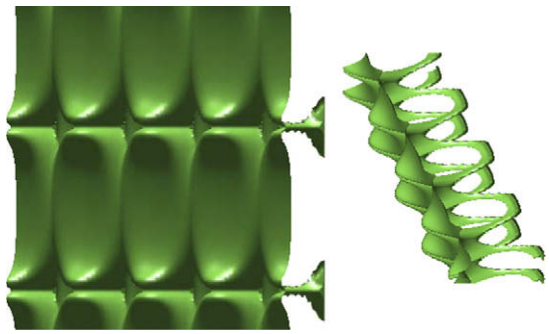

Fig. 13(e). The initially planar front after $0.75P_c$ time units of propagation and advection by the vortical flow field.

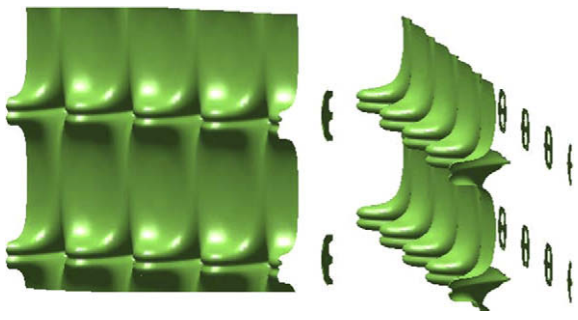

Fig. 13(f). The initially planar front after $0.875P_c$ time units of propagation and advection by the vortical flow field.

As in the previous example, a computational grid with $100 \times 100 \times 100$ nodes was used. The CFL number was set equal to 1 based on the maximum possible front speed, defined as $U_{\max} + S_L$, where $U_{\max}$ is the maximum velocity magnitude of the flow field specified in Eq. (17) and $S_L = 1$ in nondimensional units.

Figs. 13(a),13(b),13(c),13(d),13(e),13(f),13(g),13(h),13(i),13(j),13(k),13(l),13(m),13(n) show snapshots of the initially planar front at $0.25P_c$ through $1.875P_c$ time units, where $P_c = 0.125$ is the time scale of the vortical flow (as defined above); in this case the period of a fluid element advected around a vortex center in the $x - z$ plane at $y = 0$ obtained in the asymptotic limit in which the initial distance from the vortex center vanishes. Unlike in the previous example of propagation in quiescent flow, the front in this case becomes increasingly wrinkled as it propagates through the vortical flow. Fig. 13(c) shows that by $0.5P_c$ time units the front can no longer be represented analytically by a single-valued function $x = f(y, z, t)$, as in the previous example. However, the benefit of front-propagation modeling with the advection–propagation equation, Eq. (1), is that the evolution of highly corrugated and multiply-connected fronts can be computed as easily as can weakly wrinkled

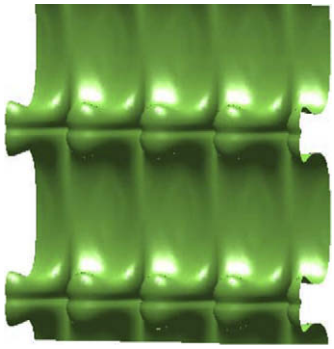

Fig. 13(g). The initially planar front after P_c time units of propagation and advection by the vortical flow field.

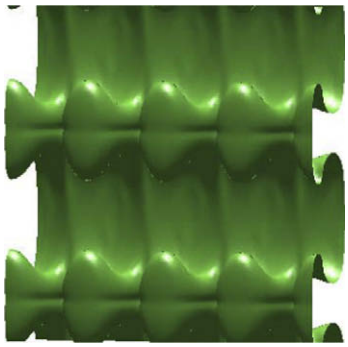

Fig. 13(h). The initially planar front after $1.125P_c$ time units of propagation and advection by the vortical flow field.

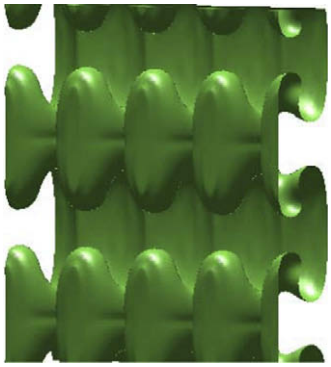

Fig. 13(i). The initially planar front after $1.25P_c$ time units of propagation and advection by the vortical flow field.

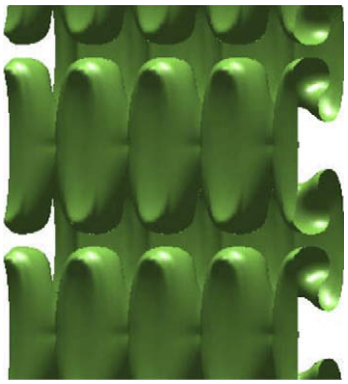

Fig. 13(j). The initially planar front after $1.375P_c$ time units of propagation and advection by the vortical flow field.

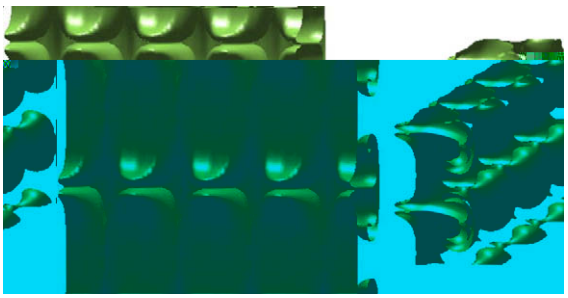

Fig. 13(k). The initially planar front after $1.5P_c$ time units of propagation and advection by the vortical flow field.

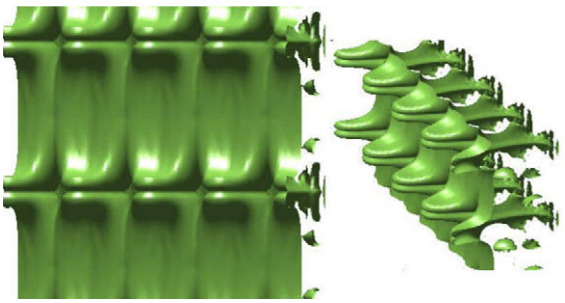

Fig. 13(l). The initially planar front after $1.625P_c$ time units of propagation and advection by the vortical flow field.

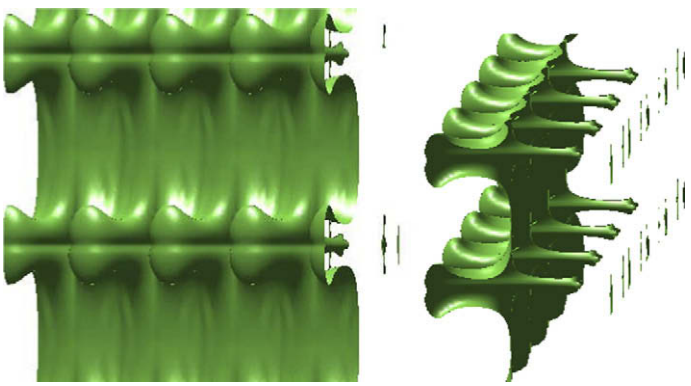

Fig. 13(m). The initially planar front after $1.75P_c$ time units of propagation and advection by the vortical flow field.

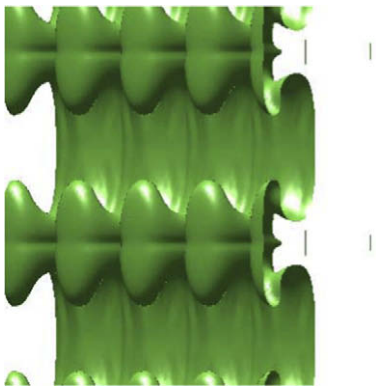

Fig. 13(n). The initially planar front after $1.875P_c$ time units of propagation and advection by the vortical flow field.

fronts [6,7,26]. Fig. 13(d) shows the development of lips behind the front that eventually collapse into rings, shown in Fig. 13(e) at $0.75P_c$ time units, due to the local normal propagation of the front. These rings later become detached from the front, by $0.875P_c$ time units (*c.f.*, Fig. 13(f)), and eventually disappear (*c.f.*, Fig. 13(g)) as a result of the inward propagation of closed front surfaces, an attribute of Eq. (1). For flame-front propagation, this is physically equivalent to the burning of detached pockets of reactants that may form behind the flame front when the flame is heavily corrugated by the flow field [26].

Another cycle of heavy front corrugation and surface detachment occurs during the next period of simulation, as shown in Figs. 13(h),13(i),13(j),13(k),13(l),13(m),13(n) for time units $1.125P_c$ through $1.875P_c$, respectively. By $2P_c$ time units of front advection and propagation the forward bulges of the front shown in Fig. 13(n) have propagated outside of the computational domain.

4. Summary

A fully three-dimensional semi-Lagrangian scheme for numerical integration of the advection–propagation equation was developed for simulation of front propagation in unsteady, nonuniform flows. Examples were provided demonstrating third-order accuracy, stability and shape preservation. The SLAP scheme was shown to be essentially conservative for the nonuniform solenoidal advection flows considered when the shape-preservation algorithm of the scheme was turned off, without notable loss of shape preservation. The capability of the scheme of capturing cusp formation and associated surface-area annihilation as well as the formation and consumption of detached closed-surface pockets behind the propagating front was also demonstrated. The CFL number based on the maximum front speed $\mathbf{U} - S_N\mathbf{n}$ is restricted to being no greater than 1, for simplicity. However, the scheme may be easily extended to allow for substantially longer time steps following traditional approaches [13,17–21]. This will be the focus of future work.

Acknowledgment

The author is grateful for support from the National Science Foundation (No. CTS-0500505) during the course of the work presented herein.

References

[1] G.H. Markstein, W. Squire, On the stability of a plane flame front in oscillating flow, The Journal of the Acoustical Society of America 27 (1955) 416.
[2] G.H. Markstein, in: G.H. Markstein (Ed.), Nonsteady Flame Propagation, The MacMillan Company, New York, 1964.
[3] F.A. Williams, Combustion Theory, Addison-Wesley, Reading, MA, 1985.
[4] A.R. Kerstein, W.T. Ashurst, F.A. Williams, Field equation for interface propagation in an unsteady homogeneous flow field, Physical Review A 37 (1988) 2728.
[5] S. Osher, J. Sethian, Fronts propagating with curvature dependent speed: algorithms based on Hamilton–Jacobi formulations, Journal of Computational Physics 79 (1988) 12–49.
[6] R.C. Aldredge, The propagation of wrinkled premixed flames in spatially periodic shear flow, Combustion and Flame 90 (1992) 121–133.
[7] R.C. Aldredge, F.A. Williams, Influence of wrinkled premixed-flame dynamics on large-scale, low-intensity turbulent flow, Journal of Fluid Mechanics 228 (1991) 487–511.
[8] J. Thuburn, Multidimensional flux-limited advection schemes, Journal of Computational Physics 123 (1996) 74–83.
[9] B.P. Leonard, A stable and accurate convective modelling procedure based on quadratic interpolation, Computer Methods in Applied Mechanics and Engineering 19 (1979) 59–98.
[10] B.P. Leonard, Universal limiter for transient interpolation modeling of the advective transport equations: the ULTIMATE conservative difference scheme, NASA Technical Memorandum 100916 (1988).
[11] B.P. Leonard, The ULTIMATE conservative difference scheme applied to unsteady one-dimensional advection, Computer Methods in Applied Mechanics and Engineering 88 (1991) 7–74.

[12] B.P. Leonard, A.P. Lock, M.K. MacVean, NIRVANA scheme applied to one-dimensional advection, International Journal of Numerical Methods for Heat and Fluid Flow 5 (1995) 341–377.
[13] B.P. Leonard, A.P. Lock, M.K. MacVean, Conservative explicit unrestricted-time-step multidimensional constancy-preserving advection schemes, Monthly Weather Review 124 (1996) 2588–2606.
[14] B.P. Leonard, M.K. MacVean, A.P. Lock, Positivity-preserving numerical schemes for multidimensional advection, NASA Technical Memorandum 106055 (1993).
[15] S.T. Zalesak, Fully multidimensional flux-corrected transport algorithms for fluids, Journal of Computational Physics 31 (1979) 335–362.
[16] P.K. Smolarkiewicz, J.A. Pudykiewicz, A class of semi-Lagrangian approximations for fluids, Journal of the Atmospheric Sciences 49 (1992) 2082–2096.
[17] A. Staniforth, J. Cote, Semi-Lagrangian integration schemes for atmospheric models – a review, Monthly Weather Review 119 (1991) 2206–2223.
[18] B.P., Leonard, Large time-step stability of explicit one-dimensional advection schemes, 1993.
[19] B.P. Leonard, Note on the von Neumann stability of explicit one-dimensional advection schemes, Computer Methods in Applied Mechanics and Engineering 118 (1994) 29–46.
[20] L.M. Leslie, R.J. Purser, Three-dimensional mass-conserving semi-Lagrangian scheme employing forward trajectories, Monthly Weather Review 123 (1995) 2551–2566.
[21] Rene J.P. Laprise, A. Plante, A class of semi-lagrangian integrated-mass (SLM) numerical transport algorithms, Monthly Weather Review 123 (1995) 553–565.
[22] J. Strain, Semi-Lagrangian methods for level set equations, Journal of Computational Physics 151 (1999) 498–533.
[23] P.K. Smolarkiewicz, The multi-dimensional Crowley advection scheme, Monthly Weather Review 110 (1982) 1968–1983.
[24] A. Taniforth, J. Côté, J. Pudykjewicz, Comments on "Swolarkiewicz's Deformational Flow", Monthly Weather Review 115 (1987) 894–900.
[25] J.A. Sethian, Level Set Methods and Fast Marching Methods: Evolving Interfaces in Computational Geometry, Fluid, Mechanics, Computer Vision, and Materials Science, Cambridge University Press, 1999.
[26] R.C. Aldredge, Premixed flame propagation in a high-intensity, large-scale vortical flow, Combustion and Flame 106 (1996) 29–40.